Hydrodynamic Instabilities in Czochralski Process of Crystal Growth – Effect of Varying The Seed to Crucible Radii Ratio

Y. Rosenstein*, P.Z. Bar-Yoseph‡

Computational Mechanics Laboratory, Faculty of Mechanical Engineering
Technion – Israel Institute of Technology, Technion city, Haifa, Israel 32000

E-mail: *ryaron@tx.technion.ac.il

E-mail: ‡merbygr@tx.technion.ac.il

Abstract. This paper deals with axisymmmetry breaking instabilities in Czochralski process of crystal growth. Numerical linear stability analysis was carried out using the axisymmetric bulk flow model. Stability diagrams of critical Grashof numbers Gr_c and frequencies ω_c dependent on aspect ratio α(=height/radius), $0.4 \leq \alpha \leq 1.0$ and Prandtl number $Pr = 0.01$ are shown. Computations were carried out using the spectral element method in the meridional plane with Fourier decomposition in the azimuthal direction. It was found that convective instability sets in through an Hopf bifuraction. First 10 modes were analyzed, only the first 5 (0,1,2,3,4) were important. Two different cases of seed to crucible radii ratio $\beta = \frac{R_x}{R_x}$ were tested. Sensitivity of mode transitions was observed at $\beta = 0.4$ and parameter range of $\alpha > 0.65$ and in some regions modes were observed approaching each other closely. For $0.4 \leq \alpha \leq 0.85$ dispersion relation analysis reveals convective instability effects while for larger α rotational effects appear.
Further more for $\beta = 0.5$ the behaviour of mode switches seems quite regular with fewer mode switches. This may imply that the parameter point $\beta = 0.4$ is a bifurcation point.

1. Introduction

Czochralski based crystal growth processes may display transitions from steady axisymmetric flow into asymmetric time dependent flows. This in turn may be a reason to inhomogeneities in the grown crystal ([12], [20]). The dynamics of the flow are complex and require the solution of the 3D time dependent flow equations coupled with the heat equation. Many published works address the 3D problem (e.g. [25]), however three dimensional, time-dependent simulations are CPU-time consuming and require the simultaneous solution of millions of equations depending on initial conditions and types of perturbations. An alternative approach employing the methods of hydrodynamic stability analysis ([17], [9], [23], [6], [4], [3]), offers considerable reduction in computer resource usage. In this approach the stability of axisymmetric steady flow with respect to 3D perturbations is analyzed and critical Grasshof number and frequency are computed.

Stability analysis of the flow in cylinders heated from below was carried out in ([9], [23]). The effects of wall conductivity on convection in cylinders are complex and were studied in [3]. Partial stability analysis for specific Prandtl number of 1.4 in Czocharalski process was carried out in [6]. This work approaches the problem using bulk flow modelling ([14]) based

on the international test ([24]). The spectral elements method pioneered by Patera [19] is used to discretize the steady axisymmetric Navier-Stokes equations coupled with the equation of energy through the Boussinesq approximation. Pressure is eliminated using the consistent penalty method ([5]). The equations are then assembled and solved using preconditioned GMRES method ([21]). Three-dimensional time-dependent perturbations are superimposed on the steady solution using Fourier decomposition of the azimuthal direction. The linear eigenvalue problem is then solved using subspace iterations ([10], [2]).
This paper is organized as follows:
In sections 2 and 3 we briefly describe the mathematical model and numerical technique employed in this work.
In section 4 results are displayed and described.
Section 5 concludes with a brief summary.

2. Mathematical formulation of the problem

We consider a co-axial cylinder-disk configuration ([14], [24]), where the disk represents the seed, both are free to rotate (see Fig. 1). The equations describing the flow are:

$$\frac{\partial \mathbf{u}}{\partial t} + (\mathbf{u}\cdot\nabla)\mathbf{u} = -\frac{\nabla p}{\rho} + \nu\nabla^2\mathbf{u} + \gamma g T \mathbf{e}_z \tag{1}$$

$$\nabla\cdot\mathbf{u} = 0 \tag{2}$$

$$\frac{\partial T}{\partial t} + (\mathbf{u}\cdot\nabla)T = \frac{\kappa}{\rho c_p}\nabla^2 T \tag{3}$$

Where ρ, ν, κ, c_p are the density, kinematic viscosity, thermal conductivity and constant pressure heat capacity of the melt respectively. γ is the coefficient of thermal expansion and $\mathbf{e_z}$ is the unit vector in the axial direction which is directed upwards. Let us denote by R_c, R_x, T_c, T_x, Ω_c, Ω_x the crucible and seed radii, temperatures and angular velocities respectively. Length, velocity and temperature are then normalized by R_c, $\frac{\nu}{R_c}$ and $(T_c - T_x)$ respectively. Thus in cylindrical coordinated the following non-dimensional equations are obtained:

$$\frac{\partial u_r}{\partial t} + (\mathbf{u}\cdot\nabla)u_r - \frac{u_\theta^2}{r} = -\frac{\partial p}{\partial r} + \left(\nabla^2 u_r - \frac{u_r}{r^2} - \frac{2}{r^2}\frac{\partial u_\theta}{\partial \theta}\right) \tag{4}$$

$$\frac{\partial u_\theta}{\partial t} + (\mathbf{u}\cdot\nabla)u_\theta + \frac{u_r u_\theta}{r} = -\frac{1}{r}\frac{\partial p}{\partial \theta} + \left(\nabla^2 u_\theta - \frac{u_\theta}{r^2} + \frac{2}{r^2}\frac{\partial u_r}{\partial \theta}\right) \tag{5}$$

$$\frac{\partial u_z}{\partial t} + (\mathbf{u}\cdot\nabla)u_z = -\frac{\partial p}{\partial z} + \nabla^2 u_z + GrT \tag{6}$$

$$\frac{1}{r}\frac{\partial (r u_r)}{\partial r} + \frac{1}{r}\frac{\partial u_\theta}{\partial \theta} + \frac{\partial u_z}{\partial z} = 0 \tag{7}$$

$$\frac{\partial T}{\partial t} + (\mathbf{u}\cdot\nabla)T = \frac{1}{\mathrm{Pr}}\nabla^2 T \tag{8}$$

Where ∇^2 and $(\mathbf{u}\cdot\nabla)$ in cylindrical coordinates are:

$$(\mathbf{u}\cdot\nabla) = u_r\frac{\partial}{\partial r} + \frac{u_\theta}{r}\frac{\partial}{\partial \theta} + u_z\frac{\partial}{\partial z} \tag{9}$$

$$\nabla^2 = \frac{1}{r}\frac{\partial}{\partial r}\left(r\frac{\partial}{\partial r}\right) + \frac{1}{r^2}\frac{\partial^2}{\partial \theta^2} + \frac{\partial^2}{\partial z^2} \tag{10}$$

With boundary conditions:

$$u_r = u_z = 0, u_\theta = rRe_c, \frac{\partial T}{\partial z} = 0 \tag{11}$$

on $z = 0$.

$$u_r = u_z = 0, u_\theta = rRe_c, T = 1 \tag{12}$$

at $r = 1$.

$$u_r = u_z = 0, u_\theta = rRe_x, T = 0 \tag{13}$$

at $0 \leq r \leq \beta, z = \alpha$.

$$\frac{\partial u_r}{\partial z} = \frac{\partial u_\theta}{\partial z} = u_z = 0, T = \frac{r - \beta}{1 - \beta} \tag{14}$$

at $\beta < r \leq 1, z = \alpha$. With pole conditions at $r = 0$ (see [8], [15] and Fig. 1):

$$u_r = u_\theta = \frac{\partial v_z}{\partial r} = \frac{\partial T}{\partial r} = 0, \ m = 0 \tag{15}$$

$$\frac{\partial u_r}{\partial r} = \frac{\partial u_\theta}{\partial r} = u_z = T = 0, \ |m| = 1 \tag{16}$$

$$u_r = u_\theta = u_z = T = 0, \ |m| > 1 \tag{17}$$

Where m is the Fourier wave number defined in equation 33. Periodicity is assumed in the azimuthal direction. The dimensionless parameters are defined as follows:

$$\alpha = \frac{H}{R_c} \text{ Aspect ratio (height/crucible radius)} \tag{18}$$

$$\beta = \frac{R_x}{R_c} \text{ Ratio of seed to crucible radii} \tag{19}$$

$$Re_x = \frac{R_c^2 \Omega_x}{\nu} \text{ Seed Reynolds number} \tag{20}$$

$$Re_c = \frac{R_c^2 \Omega_c}{\nu} \text{ Crucible Reynolds number} \tag{21}$$

$$Gr = \frac{g\gamma(T_c - T_x)R_c^3}{\nu^2} \text{ Grashof number} \tag{22}$$

$$Pr = \frac{\nu \rho c_p}{\kappa} \text{ Prandtl number} \tag{23}$$

3. Numerical method

The steady axisymmetric equations (which are obtained after omitting terms depending on θ) are discretized using the spectral element method in the meridional plane:

$$a_c(\phi_{ij}, \phi_{kl} u_r^{kl}) - b_r(\phi_{ij}, \psi_{kl} p^{kl}) + c_r(\phi_{ij}, \phi_{kl} u_r^{kl}, \phi_{mn} u_r^{mn}) + c_z(\phi_{ij}, \phi_{kl} u_z^{kl}, \phi_{mn} u_r^{mn}) - d(\phi_{ij}, \phi_{kl} u_\theta^{kl}, \phi_{mn} u_\theta^{mn}) = 0 \tag{24}$$

$$a_c(\phi_{ij}, \phi_{kl} u_\theta^{kl}) + c_r(\phi_{ij}, \phi_{kl} u_r^{kl}, \phi_{mn} u_\theta^{mn}) + c_z(\phi_{ij}, \phi_{kl} u_z^{kl}, \phi_{mn} u_\theta^{mn}) + d(\phi_{ij}, \phi_{kl} u_\theta^{kl}, \phi_{mn} u_r^{mn}) = 0 \tag{25}$$

$$a(\phi_{ij}, \phi_{kl} u_z^{kl}) - b_z(\phi_{ij}, \psi_{kl} p^{kl}) + c_r(\phi_{ij}, \phi_{kl} u_r^{kl}, \phi_{mn} u_z^{mn}) + \tag{26}$$

$$c_z(\phi_{ij},\phi_{kl}u_z^{kl},\phi_{mn}u_z^{mn}) - Gr(\phi_{ij},\phi_{kl}T^{kl}) = 0$$

$$\frac{1}{Pr}a(\phi_{ij},\phi_{kl}T^{kl}) + c_r(\phi_{ij},\phi_{kl}u_r^{kl},\phi_{mn}T^{mn}) + \tag{27}$$

$$c_z(\phi_{ij},\phi_{kl}u_z^{kl},\phi_{mn}T^{mn}) = 0$$

$$b_r^*(\psi_{ij},\phi_{kl}u_r^{kl}) + b_z^*(\psi_{ij},\phi_{kl}u_z^{kl}) = 0 \tag{28}$$

Here the superscript $*$ denotes the conjugate operator. With ϕ_{ij} and ψ_{ij} the basis functions from velocity (P_N space of polynomials with maximal degree N) and pressure (P_{N-2} space of polynomials with maximal degree $N-2$) spaces respectively (see [16], [1]). The operators in equations (24- 28) are defined in appendix A.

Applying Gauss-Lobatto quadrature on integrals (24- 28) and assembling contributions from the spectral elements we arrive at the problem:

$$(\mathbf{A} + \mathbf{C}(\mathbf{u}))\mathbf{u} + Bp - GrMT\mathbf{e}_z = 0 \tag{29}$$

$$(A + C(\mathbf{u}))T = 0 \tag{30}$$

$$B^T\mathbf{u} = 0 \tag{31}$$

Where in this context $\mathbf{u} = (u_r, u_\theta, u_z)$. Boldfaced operators $\mathbf{A}$ and $\mathbf{C}$ are the vector diffusion and convection operators respectively. A and C represent their scalar counterparts respectively. M is the discrete mass operator, B is the discrete gradient operator. To eliminate pressure, penalty method is applied to equation(31) (see [5]):

$$B^T u = -\epsilon M_{N-2} p \tag{32}$$

where $0 < \epsilon << 1$ and M_{N-2} being the mass matrix in pressure space.
The penalty parameter ϵ used in this work was $\epsilon = 10.^{-7}$. The effect of varying ϵ on eigenvalues computations is $O(\epsilon)$. The system is then linearized using Newton's method and arclength continuation is employed to march on different solution branches. Solution of the linear system is obtained using preconditioned GMRES method. The stability of steady axisymmetric solution is studied using 3D perturbations:

$$\mathbf{u}^* = \sum_{m=-\infty}^{\infty} \mathbf{u}_m(r,z)e^{im\theta+\sigma_m t} \tag{33}$$

σ_m is complex $\sigma_m = \lambda_m + i\omega_m$ with σ_m and ω_m real. When $\lambda_m \geq 0$ the flow is unstable. If as well $\omega_m = 0$ the transition is steady otherwise Hopf bifurcation exists. Substitution of perturbations in the equations of motion, the following generalized eigenvalue problem is obtained:

$$A\mathbf{x} = \sigma B\mathbf{x} \tag{34}$$

This problem is solved using the method of subspace iterations.

4. Results

4.1. Code validation

In order to test the code benchmark problems were solved. The steady state solver was compared with the works of [11] (steady convection in annular cavity) and [18] (Wheeler benchmark problem). Summary is presented in the next 2 subsections. The eigensolver was compared with the work of [22] on onset of convection in cylindrical cavity.

Table 1. Comparison of minimal stream function Ξ values in annular cavity with unit aspect ratio [11]

Parameter values	Ξ_{min}	
Ra, Re	[11].	this work
1000, 10	-0.2288	-0.2288
50000, 10	-4.122	-4.124
1000, 100	0	0

Table 2. Comparison of Critical values Gr_c for $Pr = 0.02$ and unit aspect ratio with [22]

mode	Gr_c	
	[22]	this work
0	36160	36160
2	38928	38940
1	41783	41783

4.1.1. Steady convection in annular cavity. The problem is stated in [11]. It involves the numerical study of convection in a cylindrical cavity with rotating top and inner wall (see Fig. 2). This problem addresses the cooling of rotating electric machinery. Plots of the streamlines and isotherms for $\alpha = 1$, $Ra = 1000$, $Re = 10$ are presented in Fig. 3. The minimal values of the streamfunction Ξ are compared in Table 1 for three different cases. The algorithm converges to these final values, using one global spectral element with 18×18 basis functions compared with 32×32 second order finite difference mesh used by [11].

4.1.2. Onset of convection in cylindrical cavity This problem is described in [22]. A cylindrical cavity of unit aspect ratio is heated from below with anti-symmetric temperature boundary conditions at top and bottom. The steady solution is conduction. In [22] direct numerical simulation of the time dependent Navier-Stokes equations using spatial discretization of 5 spectral elements of $7 \times 7 \times 9$ nodal points each for the x, y, z directions respectively was carried out. Linear stability analysis for modes 0, 1, 2 was carried out on this solution and compared with the results of [22] in Table 2.

The mesh was taken at 7×7 elements using 7×7 polynomial order per element,i.e 2500 nodal points total.

4.1.3. International test problem This problem is stated in [18]. For schematic representation see Fig. 1. The method used in [22] was direct numerical simulation using space discretization of 32×32 second order finite difference mesh in the meridional plane coupled with Fourier decomposition in the azimuthal direction. In this work, results computed using our code with 7×7 elements of 7×7 polynomial order each (overall 2500 nodal points) for $Re_x = 0, Re_c = 0, Pr = 0.05, \beta = 0.4, \alpha = 1$ can be seen in Fig. 4. For numerical comparison, the maximal value of the stream function computed in our work is 93.18 while [22] reports the result (using Richardson's extrapolation) 93.16. For this problem we measured the CPU time on the Technion's Compaq Alpha server ES40 with 667 MHz CPU, The times recorded were 7:50 (min) for the steady state problem and 121 (min) to scan 4 Fourier modes with 10 frequency ranges each in the eigensolver.

Table 3. Convergence of maximal stream function Ξ values for $Pr = 0.01, Gr = 2 \cdot 10^5$ and two cases of α

	Ξ_{max}			
α	3×3 el.	5×5 el.	7×7 el.	9×9 el.
0.4	16.76	16.32	16.19	16.12
0.7	[0]	40.49	40.24	40.33

[0] convergence was not achieved at the specified resolution.

Table 4. Convergence of modes $2, 3$ Gr_c values for $Pr = 0.01, \alpha = 0.65$

	Gr_c		
Mode	5×5 el.	7×7 el.	9×9 el.
2	1.55e6	1.305e6	1.302e6
3	1.05e6	1.302e6	1.298e6

4.2. Czochralski process

Simulations were carried out on the international test problem (see Fig. 1) in the range of parameters $0.005 \leq Pr \leq 0.02$, $0.4 \leq \alpha \leq 1.0$, $Re_x = 500$, $Re_c = 0$ and $\beta = 0.4,\ 0.5$. For silicon melt $\nu = 3.1 \cdot 10^{-7}\ \frac{m^2}{sec}$, $\rho = 2750\ \frac{kg}{m^3}$, $Pr = 0.01$. $Re_x = 500$ represents rotation rate of 0.6 RPM for a $50mm$ radius crucible. α ranges represent stages in the process, $beta = 0.4, ; 0.5$ is well in the range of industrial applications. Since the functional forms of the stability curves for the range of Prandtl numbers are similar only the case of $Pr = 0.01$ is presented here. Additional simulations for the first 10 modes $m = 0..9$ were carried out. Only the first 5 are relevant and will be presented here. Convergence of solver was tested for $Gr = 2 \cdot 10^5$ at $\alpha = 0.4$ and $\alpha = 0.7$ by comparing maximal values of the stream function. Our chosen Lagrangian interpolants were Legendre polynomials of the eighth degree in each direction in each element. Results are summarized in Table 3.

Eigensolver convergence was tested for the two most dangerous modes at $\alpha = 0.65$, modes $2, 3$. Results are summarized in Table 4. Table 4 shows that modes 2, 3 yield practically the same critical $Gr = 1.3 \cdot 10^6$. Based on the convergence tests, resolution of 7×7 elements using, 7×7 polynomial order per each element was chosen.

Typical steady axisymmetric picture for the range of α considered can be seen in Fig. 5 for $\alpha = 0.6$. Figs. 6 and 7 display the dependence on α of the first 5 modes for critical Gr and ω respectively at $\beta = 0.4$. The stability curves show that at $\alpha < 0.65$ mode 3 is dominant while many mode transitions occur at $\alpha \geq 0.65$ which are accompanied by either sharp changes in critical Gr or critical ω. However the changes in Gr_c and ω_c do not have to be coincident. Also modes approach each other very closely at $\alpha \geq 0.65$ as can be seen in Fig. 8. There is evidently, sensitivity of dominant modes to geometrical aspects. We proceed by observing subsections of Figs. 6 and 7. Figs. 8- 9 display modes $1, 2, 3, 4$ for $0.6 \leq \alpha \leq 0.8$. . Modes 4,2,3 compete closely for dominance at $\alpha = 0.65$. At $\alpha = 0.7$ modes 4,2 compete with each other closely. More generally no asymmetric modes $1, 3$ dominate in this section. $0.65 \leq \alpha \leq 0.8$. From Fig. 9 it can be seen that at $\alpha = 0.65, 0.75$ the frequency of mode 4 fluctuates sharply 2 orders of magnitude which is consistent with the mode switches at $\alpha = 0.65$, $\alpha = 0.75$.

Sensitivity of modes to aspect ratio can also be seen in Fig. 10 although not all modes approach each other closely. Four mode switches can be accounted for in this interval. In this interval dominant modes are asymmetric $1, 3$ except for $0.8 \leq \alpha < 0.85$. Fig 11 displays frequencies for modes $1, 2, 3, 4$ at $0.8 \leq \alpha \leq 1.0$. Sharp oscillations can be observed. It is

apparent therefore from the critical plots that mode switches in this section are accompanied by sharp fluctuations of the frequency but not of Gr_c. The final stability diagrams (lowest critical Grashof) at $Pr = 0.01$ for Gr_c and ω_c are shown in Figs. 12 and 13 respectively.

To obtain some quantitative analysis let us define the dispersion relation as function of m, α, Pr (see for example [13], page 452):

$$\omega_c = f(m, \alpha, Pr, Re_x) \tag{35}$$

A log-log plot of the curve is depicted in Fig. 14, it is obtained by taking the frequency of the most dominant mode as function of α. It is clearly seen that at sections I and II the curve is almost linear in $log(\alpha)$ with mean slope 4. In section III the curve is almost constant. In section IV the the curve is oscillatory. Thus at sections I and II one can deduce that $\omega_c = O(\alpha^4)$, at section III $\omega = f(m)$ with no dependence on α and at section IV, the behaviour is oscillatory.

The behaviour of ω_c in sections I, II, III is typical of convective instability (see for example [7]), while the behaviour of ω_c at section IV is not typical of convective instability. Figs. 15 and 16 display typical dominant temperature perturbations at $z = 0.8\alpha$, vertical velocity perturbation look very similar and hence are not displayed here. Based on the previous discussion we hypothesize that two different mechanisms dominate the instability depending on α.

From the foregoing discussion it is apparent that in the range of geometric and rotational parameters considered for $Pr > 0$ the dominating convection mechanism is mixed both hydrodynamic and thermal. At $\alpha > 0.85$ rotational effects become dominant. Figs. 17 and 18 display stability and critical frequencies dependent of α with $\beta = 0.5$, the curves seem quite regular with mode switch from 3 to 2 at $\alpha = 0.8$ again implying transition to rotational effects at $\alpha = 0.8$. However the curves are smoother and more regular with respect to the case $\beta = 0.4$ implying the specialty of parameter point $\beta = 0.4$, it is expected that as β is increased the case will be that of convection in a rotating lid-cylinder structure. Further work is required.

5. Concluding remarks

The present paper reports preliminary results of the study of three-dimensional instabilities of an axisymmetric flow model of Czochralski process. Further work would include the effects of changing the parameter values of β to obtain qualitative information. It should be emphasized that the axisymmetric model was chosen for it's simplicity and yet it's spectral behaviour is rich. From the analysis for the case of $\beta = 0.4$ it is shown that the destabilizing mechanism is mixed thermal and rotational. Modes turned out to be sensitive to changes in geometry (aspect ratio) and Pr numbers. From the dispersion relation analysis it is clear that the behaviour of the critical frequencies depends on aspect ratio. With characteristic functional forms for convective and rotational effects.

For the case of $\beta = 0.5$ more regular behaviour of the stability curves is observed implying that parameter point $\beta = 0.4$ is special. Further work is required.

Numerical convergence was tested and shows convergence of critical numbers at relatively coarse mesh of 7×7 elements of 7×7 polynomial order each.

6. Acknowledgements

This research was supported by the Samuel and Anne Tolkowsky chair at the Technion – Israel Institute of Technology. The authors would like to acknowledge the use of computer resources belonging to the High Performance Computing Unit, a division of the Inter University Computing Center, which is a consortium formed by research universities in Israel.

References

[1] M. Azaiez, A. Fikri, and G. Labrosse. A unique grid spectral solver of the nd cartesian unsteady stokes system. illustrative numerical results. *Finite Elements in Analysis and Design*, 16:247, 1994.

[2] R. Barrett, M. Berry, T. F. Chan, J. Demmel, J. Donato, J. Dongarra, V. Eijkhout, R. Pozo, C. Romine, and H. van der Vorst. *Templates for the solution of linear systems: building blocks for iterative methods*. SIAM Publications, Philadelphia, 1994.

[3] J. C. Buell and I. Catton. The effect of wall conduction on the stability of a fluid in a right circular cylinder heated from below. *ASME J. Heat Transfer*, 105:255, 1983.

[4] S. Chandrasekhar. *Hydrodynamic and hydromagnetic stability*. Clarendon, Oxford, 1961.

[5] C. Cuvelier, C. Segal, and A. A. van Steenhoven. *Finite elements methods and Navier-Stokes equations*. D. Reidel publishing company, 1986.

[6] A. Yu Gelfgat, A. Rubinov, P. Z. Bar-Yoseph, and A. Solan. Numerical study of three-dimensional instabilities in a hydrodynamic model of Czochralski growth. *J. Crystal Growth*, 275:7, 2005.

[7] A.Yu Gelfgat, P.Z. Bar-Yoseph, and A. Solan. Axisymmetry breaking instabilities of natural convection in a vertical bridgman growth configuration. *J. Crystal Growth*, 220:316, 2000.

[8] A.Yu. Gelfgat, P.Z. Bar-Yoseph, A. Solan, and T. Kowalewski. An axisymmetry-breaking instability in axially symmetric natural convection. *I. J. Trans. Phenomena*, 1:173, 1999.

[9] H. F. Goldstein, E. Knobloch, I. Mercader, and M. Net. Convection in rotating cylinder. Part 1 linear theory for moderate Prandtl numbers. *J. Fluid Mech.*, 248:583, 1993.

[10] G. H. Golub and C. F. van Loan. *Matrix computations*. Johns Hopkins, 1996.

[11] M.A. Hessami, G. de Vahl Davis, E. Leonardi, and J.A. Reizes. Mixed convection in vertical cylindrical annuli. *Int. J. Heat Mass Transfer*, 30:151, 1987.

[12] D. T. J. Hurle. *Crystal pulling from the melt*. Springer-Verlag, 1999.

[13] J. Kevorkian and J.C. Cole. *Perturbation methods in applied mathematics*. Springer-Verlag, 1981.

[14] W. E. Langlois. Buoyancy driven flows in crystal-growth melts. *Ann. Rev. Fluid Mech.*, 17:191, 1985.

[15] J.M. Lopez, F. Marques, and Jie Shen. An efficient spectral-projection method for the navier-stokes equations in cylindrical geometries II. Three dimensional cases. *J. Comp. Phys.*, 176:384, 2002.

[16] Y. Maday and A. T. Patera. Spectral element methods for the incompressible navier-stokes equations. In A.K. Noor, editor, *State-of-the-art surveys in computational mechanics*. ASME, New York, 1988.

[17] G. Neumann. Three-dimensional numerical simulation of buoyancy-driven convection in vertical cylinders heated from below. *J. Fluid Mech.*, 214:559, 1990.

[18] N.V. Nikitin and V.I. Polezhaev. Three-dimensional convective instability and temperature oscillations in Czochralski crystal growth. *Fluid Dynamics*, 34:322, 1999.

[19] A. T. Patera. A spectral element method for fluid dynamic: laminar flow in a channel expansion. *J. Comp. Phys.*, 54:468, 1984.

[20] S. M. Pimputkar and S. Ostrach. Convective effects in crystals grown from melt. *J. Crystal Growth*, 55:614, 1981.

[21] Y. Saad and M. Schultz. Gmres: A generalized minimal residual algorithm for solving nonsymmetric linear systems. *Siam J. Sci. Statist. Comput.*, 7:856, 1986.

[22] R. Touihri, H. Ben Hadid, and D. Henry. On the onset of convective instabilities in cylindrical cavities heated from below. i. pure thermal case. *Phys. Fluids*, 11:2078, 1999.

[23] M. Wanschura, V. M. Shevtsova, H. C. Kuhlmann, and H. J. Rath. Convective instability mechanisms in thermocapillary liquid bridges. *Phys. Fluids*, 7:912, 1995.

[24] A. A. Wheeler. Four test problems for the numerical simulation of flow in Czochralski crystal growth. *J. Crystal Growth*, 102:691, 1991.

[25] Q. Xiao and J. Derby. Three-dimensional melt flows in czochralski oxide growth: high-resolution, massively parallel, finite element computations. *J. Crystal Growth*, 152:169, 1995.

Appendix A. Spectral elements operators

$$a_c(f,g) = \tag{A.1}$$
$$\int_{-1}^{1}\int_{-1}^{1}[J^{-1}(\xi,\eta)r(\xi)\frac{\partial f}{\partial \xi}(\xi,\eta)\frac{\partial g}{\partial \xi}(\xi,\eta)+$$
$$J^{-1}(\xi,\eta)r(\xi)\frac{\partial f}{\partial \eta}(\xi,\eta)\frac{\partial g}{\partial \eta}(\xi,\eta) - J(\xi,\eta)\frac{fg}{r(\xi,\eta)}]d\xi d\eta$$
$$a(f,g) = \tag{A.2}$$
$$\int_{-1}^{1}\int_{-1}^{1}[J^{-1}(\xi,\eta)r(\xi)\frac{\partial f}{\partial \xi}(\xi,\eta)\frac{\partial g}{\partial \xi}(\xi,\eta)+$$
$$J^{-1}(\xi,\eta)r(\xi)\frac{\partial f}{\partial \eta}(\xi,\eta)\frac{\partial g}{\partial \eta}(\xi,\eta)]d\xi d\eta$$
$$b_r(f,q) = \int_{-1}^{1}\int_{-1}^{1} J(\xi,\eta)\frac{d\xi}{dr}\frac{\partial}{\partial \xi}[r(\xi,\eta)f(\xi,\eta)]q(\xi,\eta)d\xi d\eta \tag{A.3}$$
$$b_z(f,q) = \int_{-1}^{1}\int_{-1}^{1} r(\xi,\eta)J(\xi,\eta)\frac{d\eta}{dz}\frac{\partial f}{\partial \eta}(\xi,\eta)q(\xi,\eta)d\xi d\eta \tag{A.4}$$
$$c_r(f,g,h) = \int_{-1}^{1}\int_{-1}^{1} r(\xi,\eta)J(\xi,\eta)\frac{d\xi}{dr}fg\frac{\partial h}{\partial \xi}(\xi,\eta)d\xi d\eta \tag{A.5}$$
$$c_z(f,g,h) = \int_{-1}^{1}\int_{-1}^{1} r(\xi,\eta)J(\xi,\eta)\frac{d\eta}{dz}fg\frac{\partial h}{\partial \eta}(\xi,\eta)d\xi d\eta \tag{A.6}$$
$$d(f,g,h) = \int_{-1}^{1}\int_{-1}^{1} J(\xi,\eta)fghd\xi d\eta \tag{A.7}$$

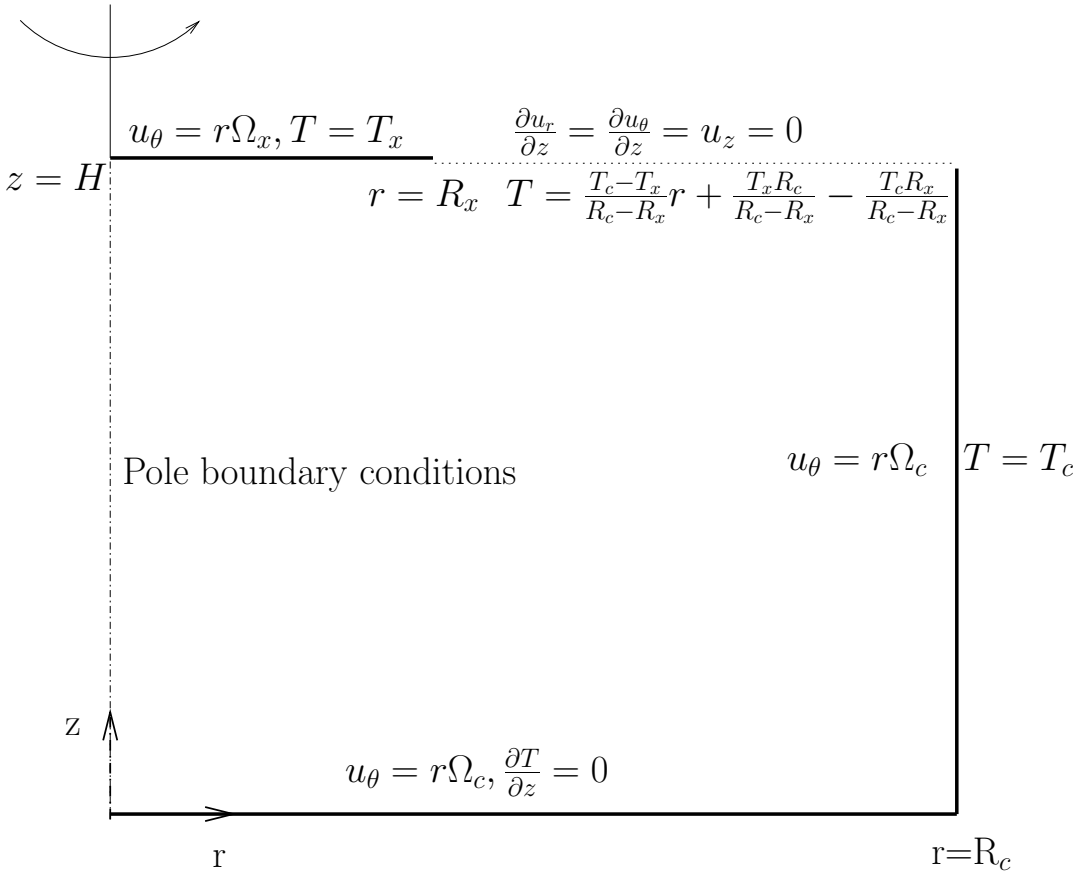

Figure 1. Czochralski process of crystal growth ([24]) - sketch of the problem

Appendix: Figures

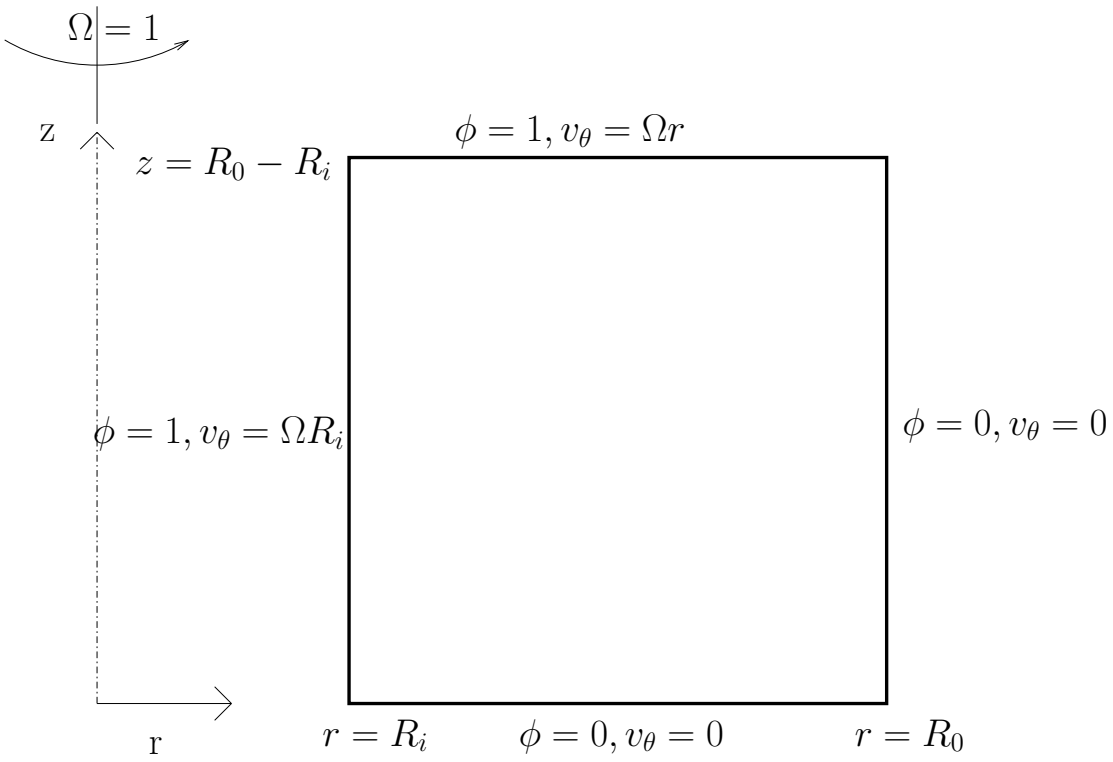

Figure 2. Annular cavity with rotating top and inner wall ([11]) - sketch of the problem

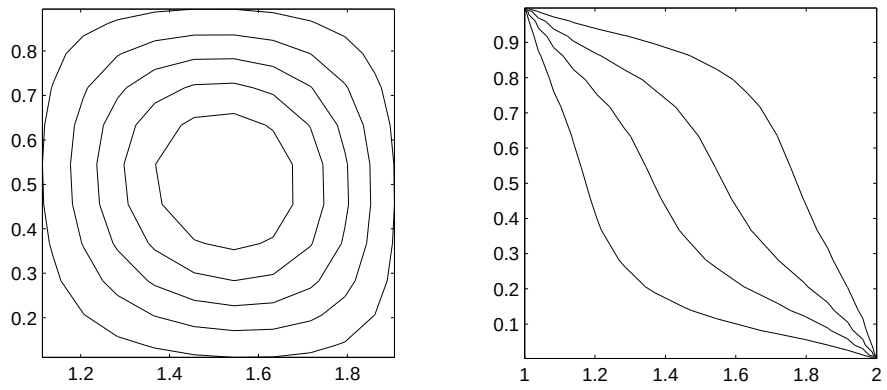

Figure 3. Annular cavity, streamlines (left) and isotherms (right), Ra=1000, Re=10

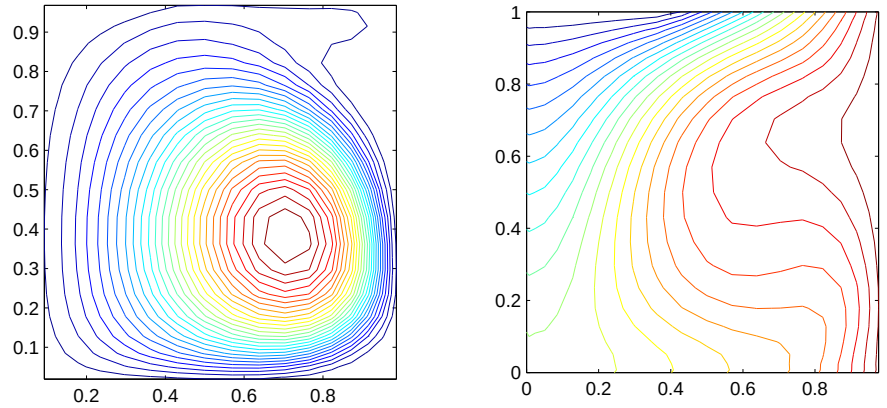

Figure 4. Wheeler benchmark, streamlines (left) and isotherms (right) for $Gr = 10^6$

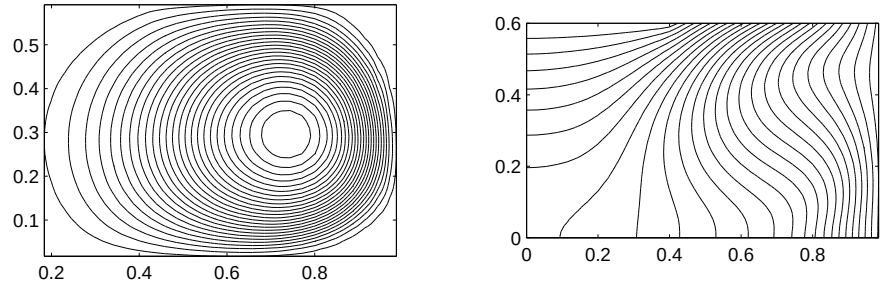

Figure 5. Streamlines (left) and isotherms (right) for $Pr = 0.01$, $\alpha = 0.6$, $Gr = 1.3 \cdot 10^6$

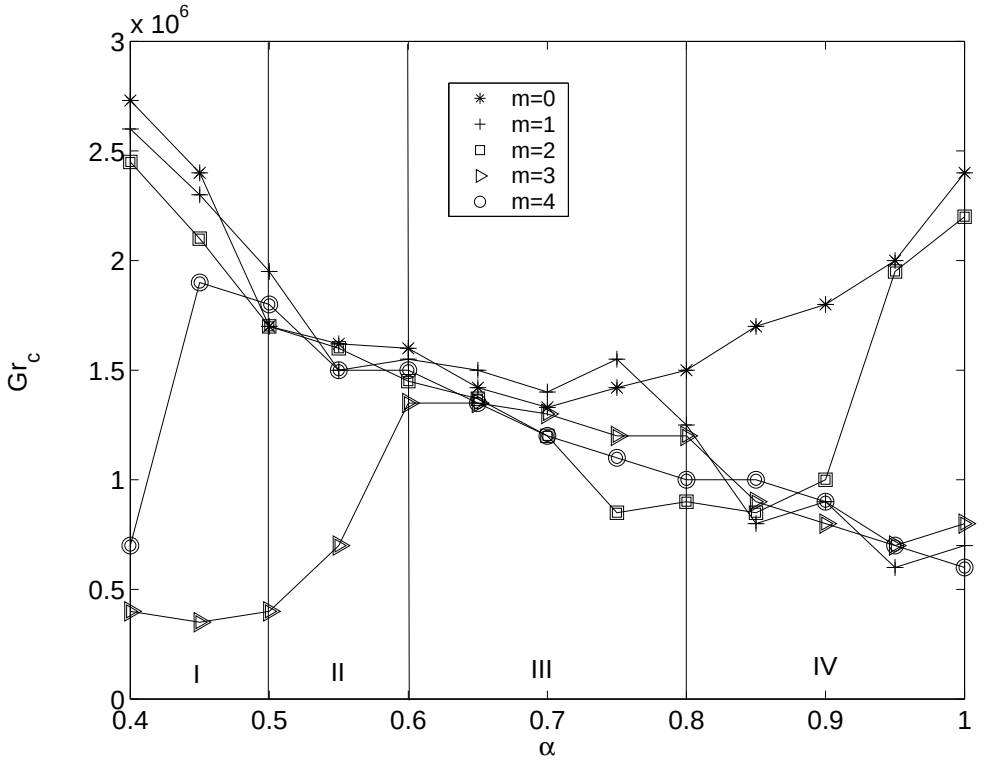

Figure 6. Critical Gr numbers for $Pr = 0.01$ with wavenumber as parameter, $Re_x = 500, Re_c = 0, \beta = 0.4$

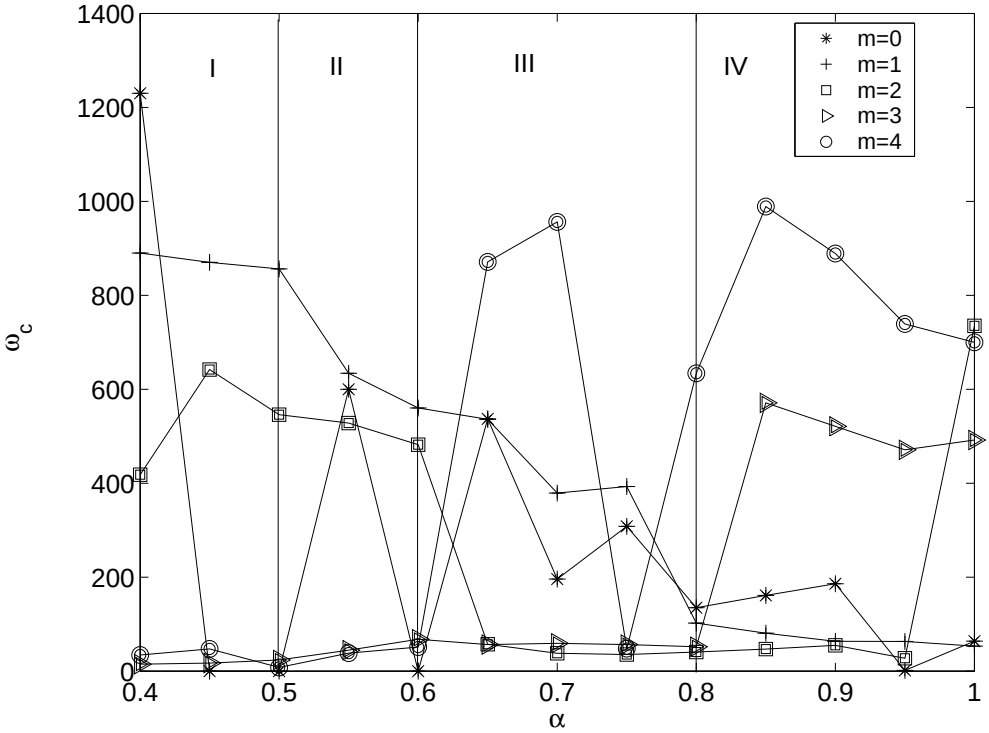

Figure 7. Critical frequencies for $Pr = 0.01$ with wavenumber as parameter, $Re_x = 500, Re_c = 0, \beta = 0.4$

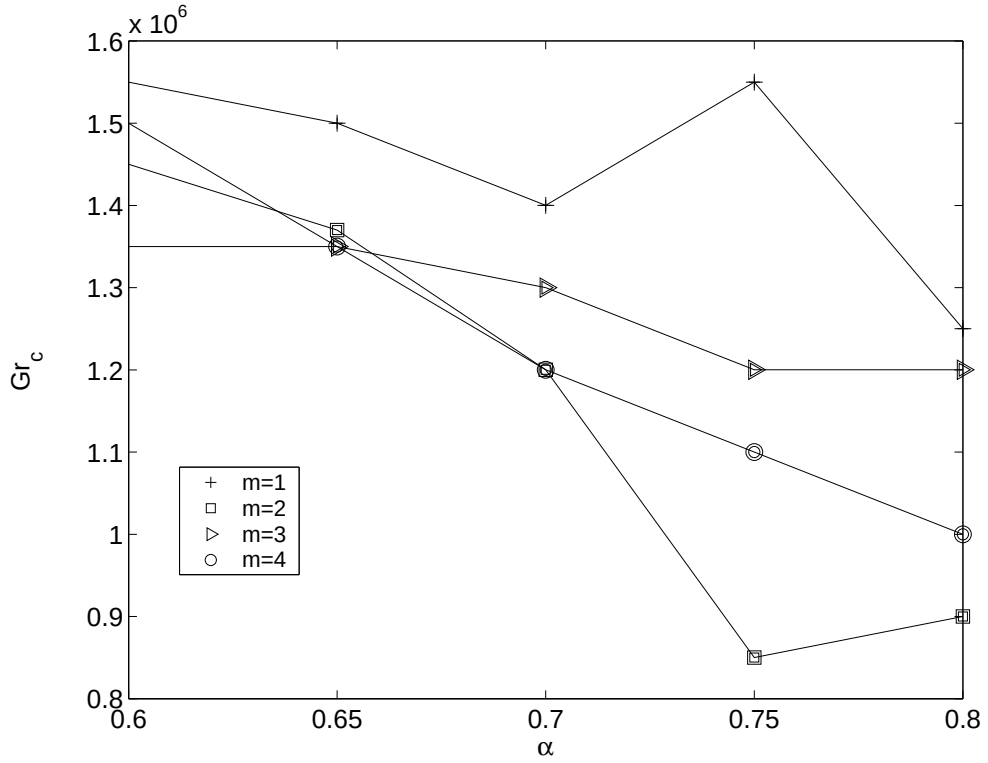

Figure 8. Section III of fig. 6

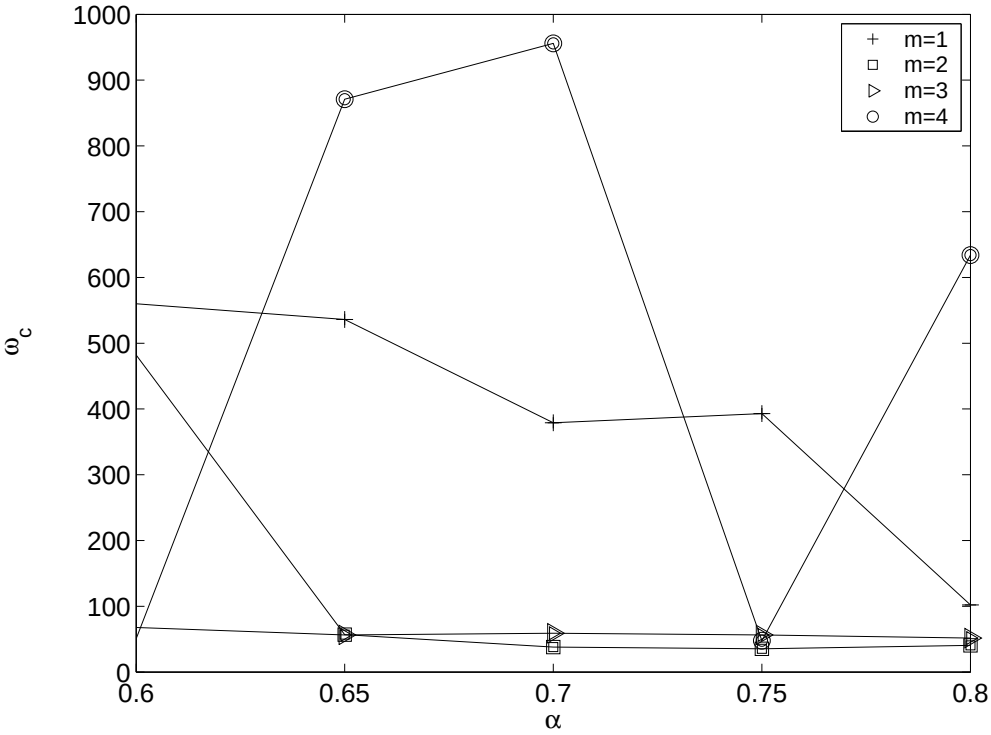

Figure 9. Section III of fig. 7

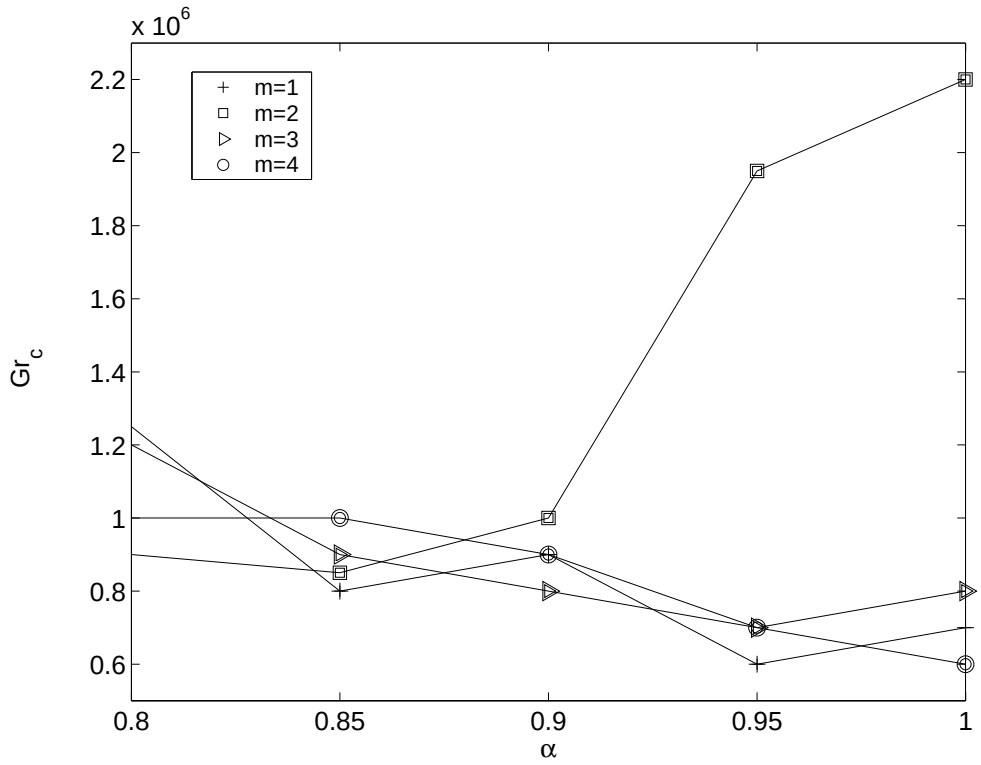

Figure 10. Section IV of fig. 6

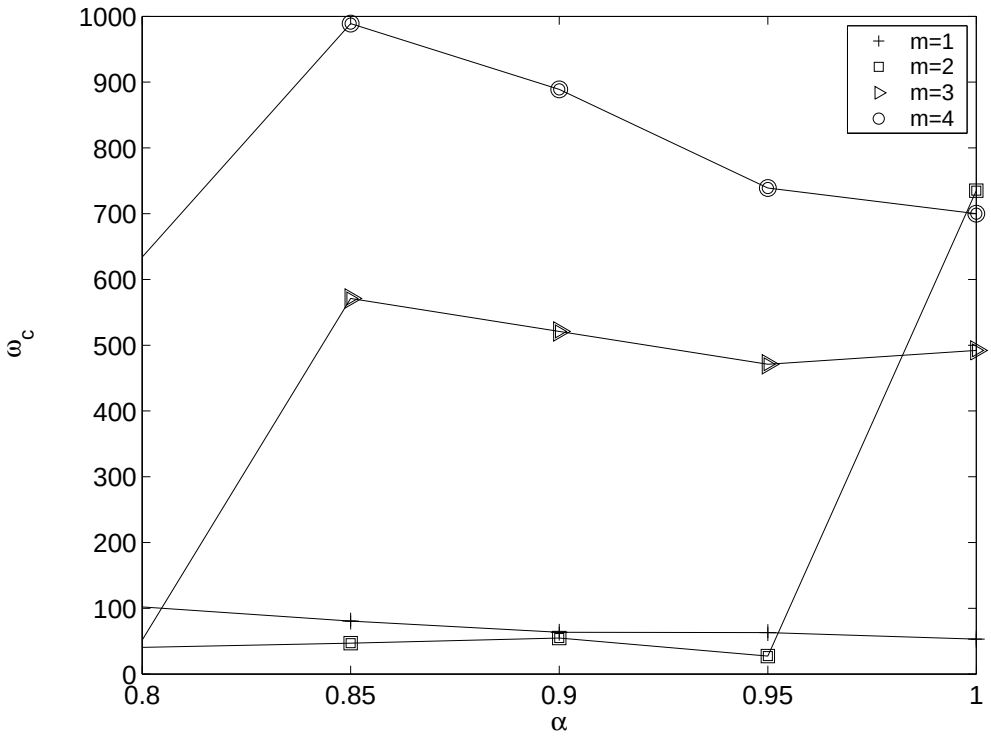

Figure 11. Section IV of fig. 7

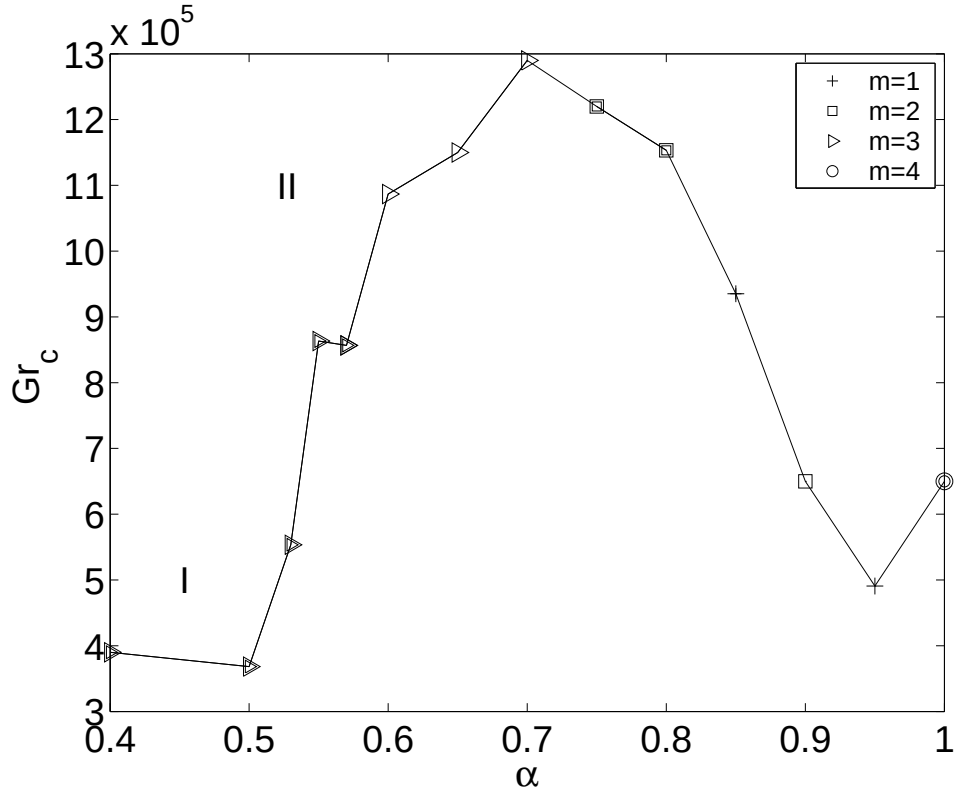

Figure 12. Stability diagram showing critical Gr numbers with $Pr = 0.01$, $Re_x = 500, Re_c = 0, \beta = 0.4$

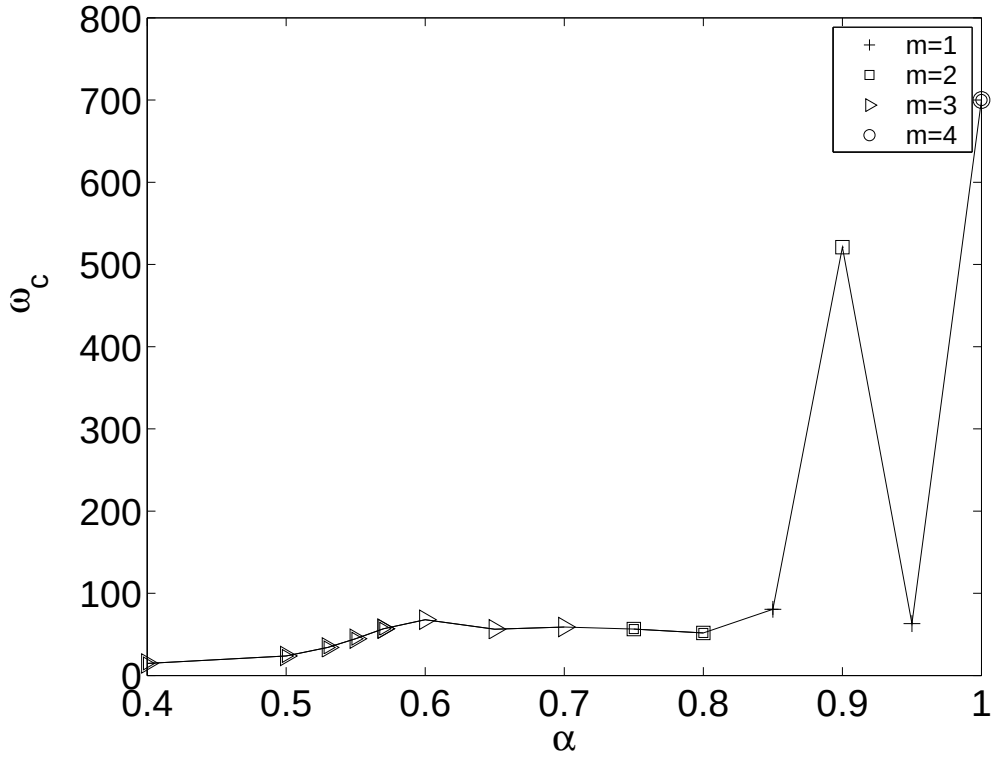

Figure 13. Critical frequencies with $Pr = 0.01,\ Re_x = 500, Re_c = 0, \beta = 0.4$

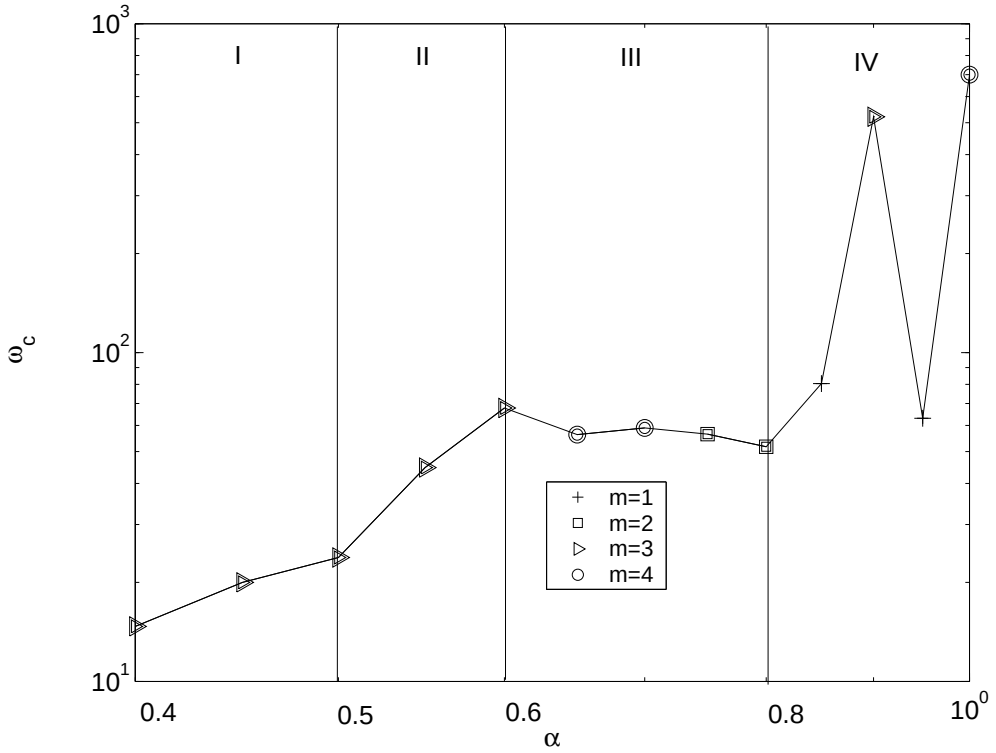

Figure 14. log-log plot of the critical frequencies as function of α for $Pr = 0.01$, $Re_x = 500, Re_c = 0, \beta = 0.4$

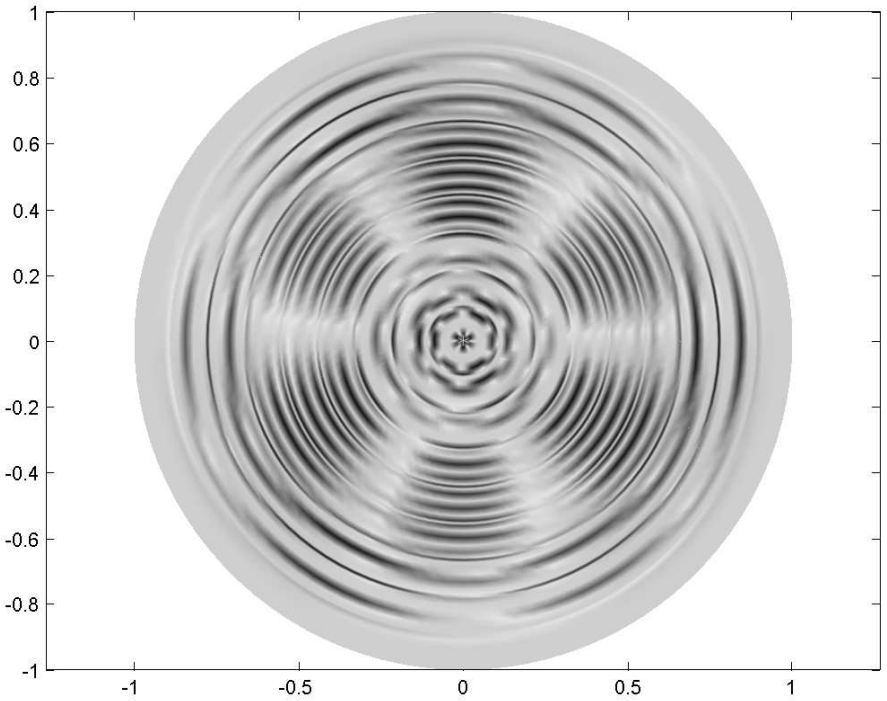

Figure 15. Temperature perturbation at $z = 0.36$ for $Pr = 0.01$, $\alpha = 0.45$, $m = 3$

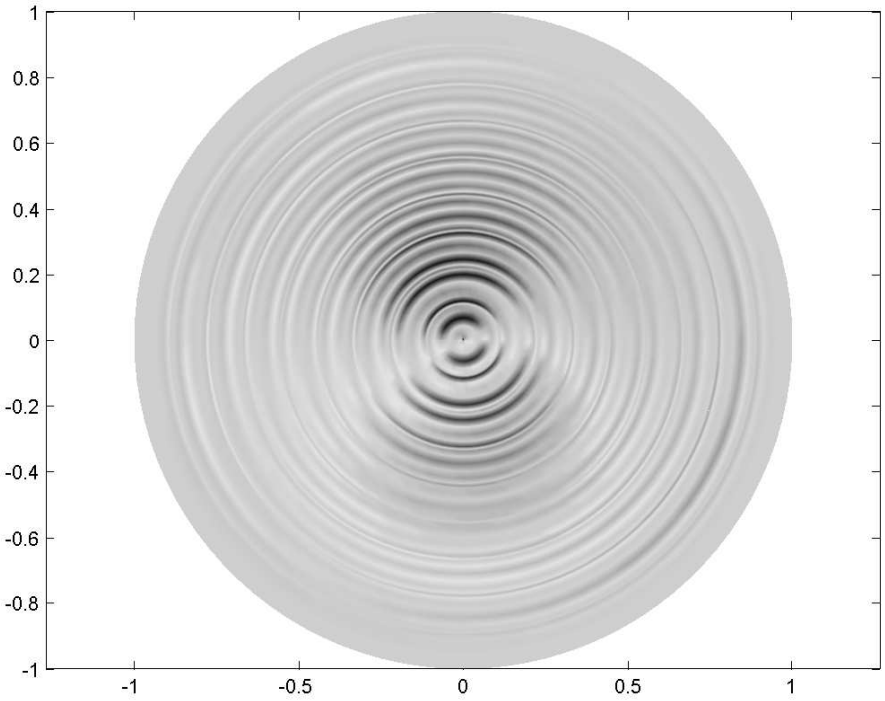

Figure 16. Temperature perturbation at $z = 0.68$ for $Pr = 0.01$, $\alpha = 0.85$, $m = 1$

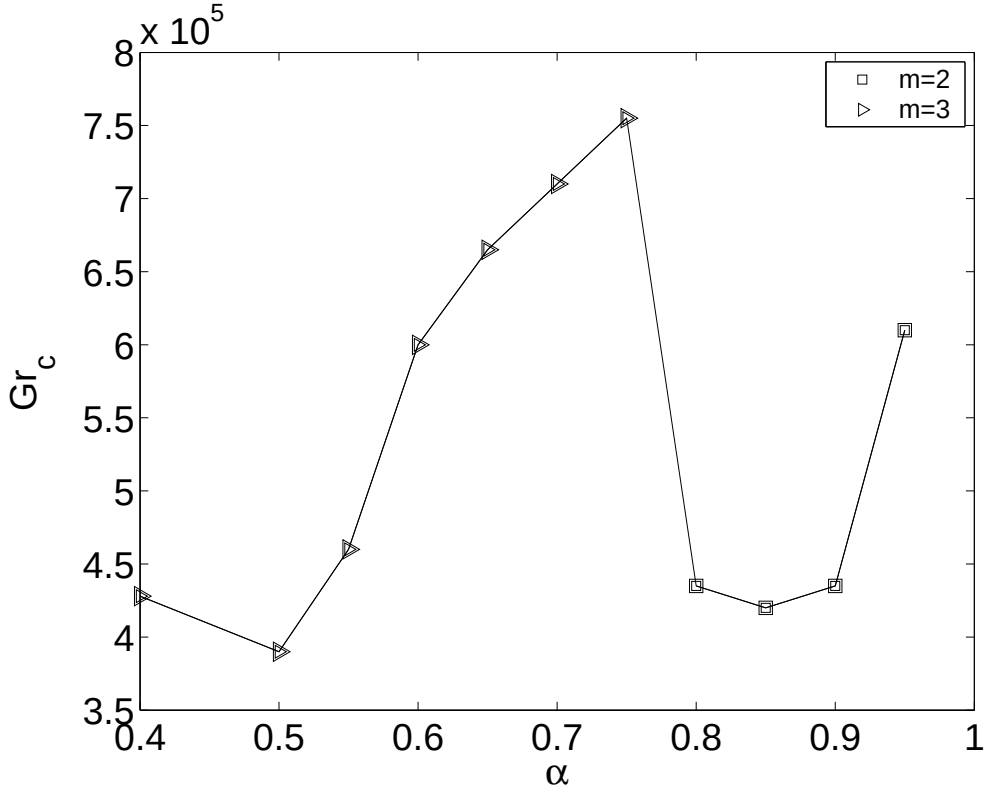

Figure 17. Stability diagram showing critical Gr numbers for $\beta = 0.5$ with $Pr = 0.01$, $Re_x = 500, Re_c = 0$

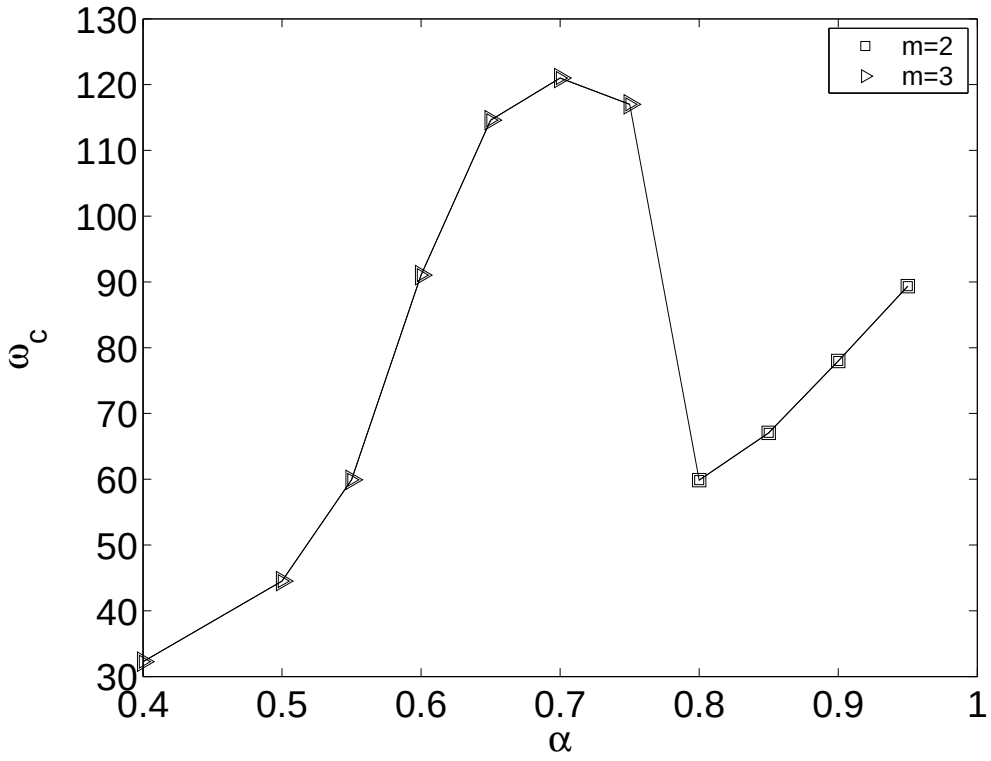

Figure 18. Critical frequencies for $\beta = 0.5$ with $Pr = 0.01$, $Re_x = 500, Re_c = 0$